Geophys. J. Int. (2008) **172,** 842–860 doi: 10.1111/j.1365-246X.2007.03645.x

Upscaling of elastic properties of anisotropic sedimentary rocks

Irina O. Bayuk,[1] Mike Ammerman[2] and Evgeni M. Chesnokov[3]

[1]*Institute of Physics of the Earth, Russian Academy of Sciences, Moscow, Russia. E-mail: irina_bayuk@mail.ru*
[2]*Devon Energy Corporation, Oklahoma City, Oklahoma, USA*
[3]*School of Geology and Geophysics, College of Earth and Energy, University of Oklahoma, Norman, Oklahoma, USA*

Accepted 2007 October 2. Received 2007 September 17; in original form 2006 October 15

SUMMARY

In this paper, the term 'upscaling' means the theoretical prediction of rock's elastic properties at lower frequency (seismic or cross-well data) using higher frequency logging data on sonic velocities (V_P, V_{S1} and V_{S2}), porosity and density. The mineral composition and water saturation derived from other logs are used. Due to the special treatment of sonic logging data provided by the dipole sonic probe, all the sonic velocities are obtained in the principal coordinate system of the rock's stiffness tensor. The upscaling procedure includes two steps. The first step involves the solution of an inverse problem on reconstruction of the parameters of the rock's microstructure from the logging data. The inversion is based on the effective medium theory. As a result of the inverse problem solution, the effective stiffness tensor is found for depths at which the sonic wave velocities are measured. At the second step, the velocities of waves at given lower frequencies are calculated as propagating in a layered medium. The number of layers in the medium depends on the given frequency and logging step. Each layer of the medium has the stiffness tensor found at the first step.

This upscaling procedure has been applied to a wellbore for which the dipole sonic data are available. The rocks penetrated by the well are shales. In general, the resulting medium exhibits orthorhombic symmetry at sonic frequency. This symmetry results from the preferential orientation of clay platelets and grain-related cracks and vertical cracks. The existence of the latter is indicated by the dipole sonic tool. Depending on the microstructure parameters (orientation of clay platelets and cracks, pore/crack connectivity and shale mineralogical composition), the shales, at lower frequency, have either transversely isotropic symmetry (with the vertical axis of symmetry, a.k.a. VTI) or orthorhombic symmetry.

Key words: Elasticity and anelasticity; Seismic anisotropy.

1 INTRODUCTION

The elastic properties of sedimentary rocks depend on the scale at which they are measured. The problem of predicting the elastic wave velocities at a large scale from the velocities at a smaller scale is one of the key geophysical problems. Note that not only velocities change when going to another scale but also the anisotropy type of the medium can be different at different scales.

Valcke *et al*. (2006) solved a problem of predicting the elastic properties of sedimentary rocks at seismic frequencies from their microscopic structure. They quantified the preferred orientation of minerals in different sedimentary rocks using the Electron Backscattering Diffraction and X-ray Texture Goniometry. The effective stiffness tensor of the polycrystalline aggregates were calculated with the Voigt–Reuss–Hill averaging. The averaged stiffness tensor was suggested to be considered as the tensor at the seismic frequency for rocks without layering. For fine-layered siltstone, the authors then apply a Backus-type averaging. As a result, they theoretically estimated a contribution of preferred orientation of different minerals in the seismic anisotropy. In the study, the anisotropy caused by the orientation of phyllosilicates in a shale sample reaches 12 per cent. The authors did not analyse the effect of pores and oriented cracks on the elasticity. It should be noted that the elastic properties of certain shales also can be greatly affected by pores and cracks, and that the latter contribute considerably to the rock's anisotropy, specifically in shales (Vernik 1993).

A very interesting method of upscaling has been suggested by Chapman (2003). He has developed a method allowing the fluid communication between pores and microcracks at the scale of about hundred microns with mesoscale fractures at the centimetre scale, which results in dispersion of elastic wave velocities in the seismic frequency range. This method allows one to estimate, at a given frequency, the effective stiffness tensor of a porous cracked medium with a system of aligned fractures. The result is dependent on the fracture length. The limitation of this method is that it is applicable to rocks whose symmetry is transversely isotropic and higher (isotropic and cubic).

Sayers (1998) considered the upscaling of data provided by sonic logs. Two types of upscaling were analysed in this work: (1) performed with the Backus average (1969) for laterally continuous

layers and (2) with the Ponte Castaneda and Willis method (1995) for layers of finite thickness-to-width ratio. Sayers pointed out that these two types of upscaling give different results, and the lateral heterogeneity of the formation should be taken into consideration. However, he did not take into account the anisotropy of rocks (a shale was considered) at sonic frequency.

Bayuk *et al*. (2003a,b) solved a similar problem of upscaling the sonic data with the help of the pair correlation function method, which gives a possibility to predict the elastic wave velocities at a given frequency. In this case, the frequency dependence is caused by scattering. The technique developed allows one to apply the method only for isotropic layers.

In this work, we suggest an upscaling of logging data with allowance made for the layers' anisotropy, which is important for shales. In the upscaling we assume that the layers' width is much greater than their thickness, which allows us to apply the Backus-type averaging, since we have no information on the lateral heterogeneity. For the upscaling, we use dipole sonic logs giving two shear waves propagating in the vertical direction. We assume that the shear wave splitting is caused by vertical cracks in the vicinity of the wellbore. The existence of vertical cracks in shales is debatable. However, vertical cracks were observed in Devonian shales of the Appalachian basin (Vernik 1994), and we should not exclude them from this consideration. Since shales are of VTI symmetry, the presence of vertical cracks leads to orthorhombic symmetry.

The use of a dipole sonic probe provides new possibilities for solving the upscaling problem, since this allows one to generalize the symmetry of rocks under study to orthorhombic symmetry. In addition, the information of shear wave splitting makes it possible to more precisely reconstruct the pore/crack geometry as compared to the case of single V_S measurement. This reconstruction is based on theoretical modelling of macroscopic elastic properties of rock with the help of effective medium theory (EMT) assuming that the pore/crack shape is ellipsoidal. In such a modelling, shear wave velocity splitting is attributed to vertical fractures (with horizontal axis of symmetry) whose size is smaller than the length of shear wave at sonic frequency of 2 kHz (from 1 to 2.2 m), that is, the facture size is not greater than 10–15 cm. The transmitter-receiver spacing in the probe is 4 m, that is, somewhat greater than the shear wavelength. In this case, the measured velocities can be considered as propagating in the effective medium (i.e. long wavelength approximation is applicable). The solution to the upscaling problem proposed in this paper includes two steps described below.

Step 1: The inverse problem on rock's microstructure reconstruction is solved for each logging depth. This reconstruction is based on optimization of a functional which is the sum of squared differences between experimental velocities and theoretical velocities calculated by formulas of EMT. The theoretical formulas include a set of parameters considered as unknown (or poorly known). The solution of the inverse problem gives the parameters producing the best fit between the theoretical and experimental velocities. The theoretical model used in the inverse problem is described in Section 1. After the optimum parameters are found, a complete stiffness tensor can be calculated for each logging depth. The tensor has, in general, orthorhombic symmetry.

Step 2: This step includes solution of the upscaling problem for a layered medium consisting of anisotropic layers whose elasticity is described by the stiffness tensors found for each depth from optimum parameters provided by the inverse problem solution (step 1). The upscaled stiffness tensor is found with the Backus-type average. In a general case, this tensor has orthorhombic symmetry.

Hereinafter, we use the term 'pore/crack' to characterize all voids existing in rock. As a rule, the term 'crack' is related to non-isometric voids with small openings.

2 RECONSTRUCTION OF SHALE'S STIFFNESS TENSOR FROM LOGGING DATA

2.1 Physical model of shale

Shales are anisotropic rocks whose anisotropy is generally caused by the preferential orientation of clay platelets and cracks. These two principal reasons for shale anisotropy (as a single reason or combined effect of both) were considered by Kaarsberg (1959), Vernik (1993), Hornby *et al*. (1994), Johnston & Christensen (1995), Vernik & Liu (1997), Lonardelli *et al*. (2007) and Wenk *et al*. (2007). Also, kerogen is commonly present in shales, which forms a network surrounding the clay particles (Vernik 1994). The model of shale has been constructed in the following steps (see Fig. 1). At the first step, clay particles are embedded in a kerogen matrix. It is assumed that aspect ratio (AR) of platelets is 1e-5. This corresponds to the case when the platelet of 1-mm length has a thickness of ten nanometers. The thickness is comparable to the thickness of illite platelets (Katahara 1996). Then, at the second step, grains of silt-sized minerals and grain-related pore/cracks are inserted into the kerogen-clay matrix. At the third step, the pieces of material obtained at the second step are considered as 'monocrystals'. These monocrystals are rotated around the vertical axis such that the '*c*' axes of them draw a cone around the vertical axis. The rotation is described by the Gaussian law with zero mean and a non-zero standard deviation specifying the deviation of the '*c*' axes from the vertical direction. Hereinafter we call this standard deviation 'Gaussian sigma'. The medium resulting from the third step has transversely isotropic symmetry. If shear wave splitting is observed in the dipole sonic measurements, at the fourth step, a system of thin vertical cracks is inserted into the rock. We assume that the symmetry plane of the vertical cracks is in the *XZ* plane of the Earth's coordinate system (with the *Z*-axis being the vertical axis). The resulting medium is, in general, of orthorhombic symmetry. The shape of both grain-related pore/cracks and vertical cracks is assumed to be ellipsoidal. The ellipsoids are penny-shaped ellipsoids of revolution (with two large equal semi-axes in the crack plane and small semi-axis normal to the crack plane). We consider the cracks as penny-shaped ellipsoids since this shape is more commonly met in reality than the needle-shape. Certainly, in reality, it is difficult to find cracks with two equal axes, and the approximation of cracks by a general ellipsoid seems to be more acceptable. However, according to theoretical modelling, the elastic properties are generally controlled by the ratio of minimum-to-maximum axes of crack if the intermediate and maximum axes are not significantly different. Consequently, the approximation of pore/crack shape by ellipsoid of revolution is commonly used. In our model, all pore/cracks are assumed to be connected, and the degree of their connectivity is described by a parameter called 'friability' (Bayuk & Chesnokov 1998).

The unknown parameters of the shale model are as follows: kerogen amount, AR of grain-related pore/cracks, friability, Gaussian sigma, volume concentration of vertical cracks and AR of vertical

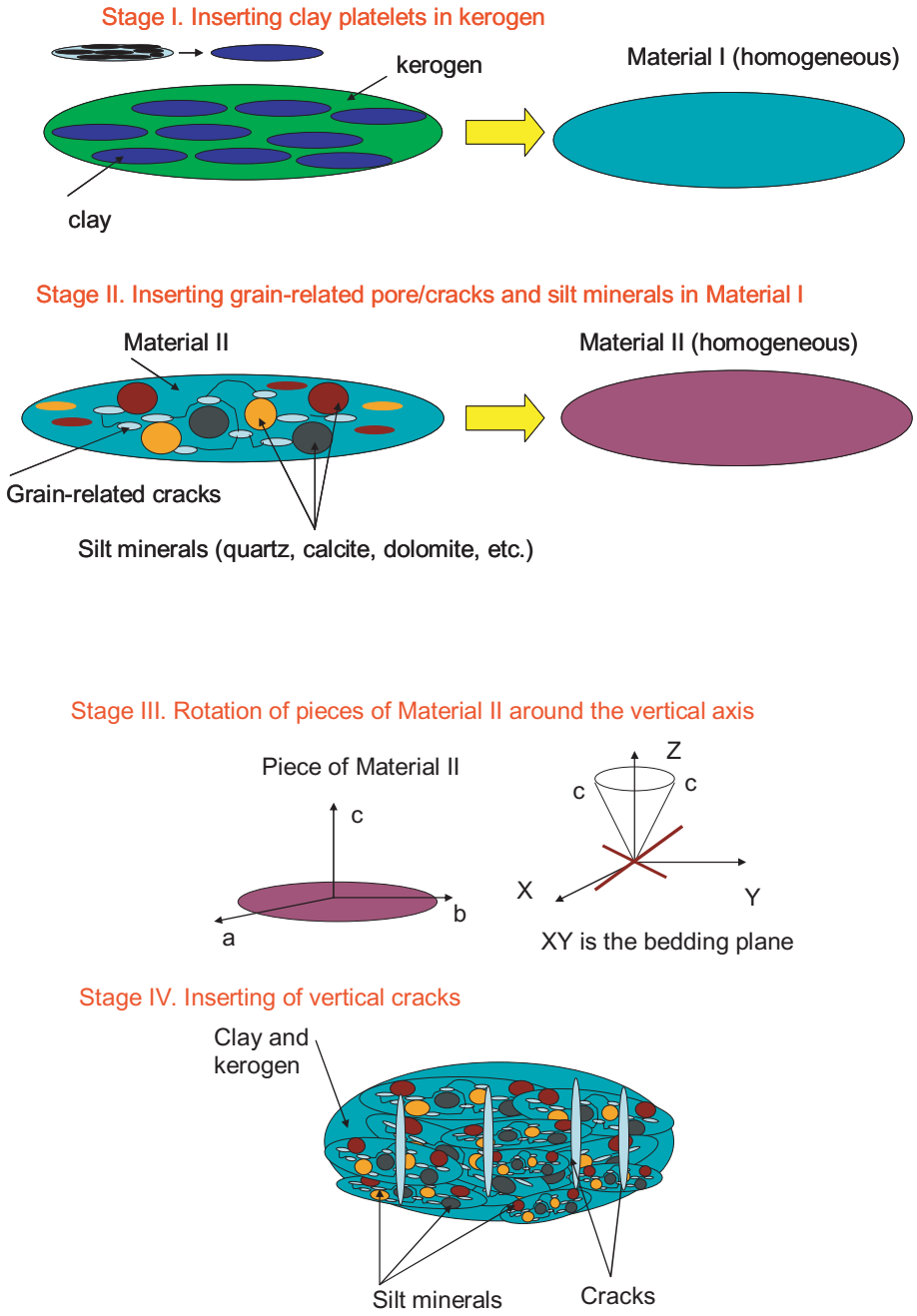

Figure 1. Stages of the shale model construction.

cracks. In addition, we also perform a correction of the logging porosity within 2 per cent.

2.2 Method of the problem solution

The pore/crack geometry is reconstructed with the help of non-linear optimization based on the generalized singular approximation (GSA) method of EMT (Shermergor 1977; Bayuk & Chesnokov 1998). Below we give a derivation of the GSA formulas following Shermergor (1977). In what follows, we use the term 'inclusions' for the mineral grains and all voids (grain-related pore/cracks and vertical cracks). The GSA method is based on the comparison of displacement fields in a heterogeneous body whose stiffness tensor is to be determined and in a homogeneous, so-called, comparison body. The stiffness tensor of the comparison body is known. It is assumed that the strain field in the both bodies obeys the Hooke law, that is,

$$\begin{aligned} \mathbf{Lu} &= -\mathbf{f}\left(L_{il} \equiv \nabla_j C_{ijkl} \nabla_k\right), \\ \mathbf{L^C u^C} &= -\mathbf{f}\left(L^C_{il} \equiv \nabla_j C^C_{ijkl} \nabla_k\right), \end{aligned} \tag{1}$$

where C and C^C, are, respectively, the stiffness tensors of a heterogeneous body and a comparison body; $\mathbf{u}$ is the displacement vector (hereinafter, the superscript 'c' indicates that the variable is related to the comparison body); $\mathbf{f}$ is the density of volume forces; ∇_a is the derivative of a function with respect to coordinate a.

According to eq. (1), we can write

$$\mathbf{L^C u'} = -\mathbf{L' u}, \tag{2}$$

where $\mathbf{u}' \equiv \mathbf{u} - \mathbf{u^C}$, and $\mathbf{L}' \equiv \mathbf{L} - \mathbf{L^C}$.

If we determine the Green's tensor $\mathbf{G}$ of operator $\mathbf{L^C}$ as follows

$$\mathbf{L^C G} = -\mathbf{I}\delta(r), \tag{3}$$

where $\mathbf{I}$ is the fourth-rank unit tensor, and δ is the Kronecker delta, the solution to (2) is found in the form

$$\mathbf{u'} = \mathbf{G} * \mathbf{L'u}. \tag{4}$$

Rewriting eq. (4) in terms of strain, we have

$$\begin{aligned}\varepsilon'_{ij} &= \oint G_{k(i,j)}(\mathbf{r}-\mathbf{r}_1)C'_{klmn}(\mathbf{r}_1)\varepsilon_{mn}(\mathbf{r}_1)\mathrm{d}S_l^1 \\ &\quad + \int G_{k(i,j)l}(\mathbf{r}-\mathbf{r}_1)C'_{klmn}(\mathbf{r}_1)\varepsilon_{mn}d\mathbf{r}_1 \\ &\equiv \left(Q^0_{ijkl} + Q_{ijkl}\right)C'_{klmn}\varepsilon_{mn},\end{aligned} \tag{5}$$

where $\mathbf{C}' \equiv \mathbf{C} - \mathbf{C^c}$. In eq. (5), the symmetrization is carried out over the indices in parenthesis. It can be shown that for bodies of rather great size the term $\mathbf{Q}^0$ can be omitted. If we consider a volume of rock large enough compared to the heterogeneity size, we can neglect this term. In our model, we assume that the heterogeneities are mineral grains and voids.

After some algebraic rearrangements, from eq. (5) we can obtain a relation between the strain field at a point $\mathbf{r}$ in the heterogeneous body and the volumetric average of strain in the body:

$$\varepsilon = \left(\mathbf{I} - \mathbf{QC}'\right)^{-1}\left\langle\left(\mathbf{I} - \mathbf{QC}'\right)^{-1}\right\rangle^{-1}\langle\varepsilon\rangle\,. \tag{6}$$

In eq. (6), the angular brackets $\langle\rangle$ mean volume averaging. Applying to (6) the definition of effective stiffness tensor

$$\langle\boldsymbol{\sigma}\rangle = \mathbf{C}^*\langle\varepsilon\rangle\,, \tag{7}$$

we obtain

$$\mathbf{C}^* = \left\langle\mathbf{C}(\mathbf{I} - \mathbf{QC}')^{-\mathbf{1}}\right\rangle\left\langle(\mathbf{I} - \mathbf{QC}')^{-\mathbf{1}}\right\rangle^{-1}. \tag{8}$$

In formula (8), $\mathbf{Q}$ is an integral operator. Consequently, the effective stiffness tensor is an integral operator as well. In the GSA method, the operator $\mathbf{Q}$ is replaced by a constant tensor $\mathbf{g}$**.** In order to do this, we write the operator $(\mathbf{I} - \mathbf{QC}')^{-1}$ in the form of series

$$(\mathbf{I} - \mathbf{QC}')^{-1} = \sum_{n=0}^{\infty}\left(\mathbf{QC}'\right)^n. \tag{9}$$

The operator $\mathbf{Q}$ can be replaced by a constant tensor $\mathbf{g}$ if the following condition is met

$$\begin{aligned}Q_{ijkl}C'_{klpq} &\equiv \int G_{k)(i,j)(l}(\mathbf{r}-\mathbf{r}_1)C'_{klpq}(\mathbf{r}_1)\mathrm{d}\mathbf{r}_1 = g_{ijkl}C'_{klpq}(\mathbf{r}), \\ G_{k)(i,j)(l} &\equiv \frac{G_{k(i,j)l} + G_{l(i,j)k}}{2},\end{aligned} \tag{10}$$

where the notation *(i, j)* means symmetrization over indices *i* and *j*.

Condition (10) is satisfied if we set

$$G_{k)(i,j)(l} \approx g_{ijkl}\delta(\mathbf{r}), \tag{11}$$

that is, we neglect the coordinate dependence of the second derivative of the Green's function. In this case, according to relation (6), the strain is homogenized within each heterogeneity type. This is applicable if there is no far order in the medium, and heterogeneity of each type is at almost the same conditions in various parts of the body volume. Now relation (8) can be rewritten as follows

$$\mathbf{C}^* = \left\langle\mathbf{C}\left(\mathbf{I} - \mathbf{gC}'\right)^{-\mathbf{1}}\right\rangle\left\langle(\mathbf{I} - \mathbf{gC}')^{-\mathbf{1}}\right\rangle^{-1}. \tag{12}$$

Note that Willis (1977) obtained the same formula but using another way of its derivation. For each type of inclusions, the tensor $\mathbf{g}$ has the form (for simplicity, the inclusion index *i* is omitted):

$$\begin{aligned}g_{kmln} &= \tilde{a}_{k)(l,n)(m}, \\ \tilde{a}_{k)(l,n)(m} &\equiv \frac{1}{4}(a_{klnm} + a_{mlnk} + a_{knlm} + a_{mnlk}), \\ \tilde{a}_{kmln} &= -\frac{1}{4\pi}\int n_{mn}\Lambda^{-1}_{kl}\sin\theta\,\mathrm{d}\theta\,\mathrm{d}\varphi,\end{aligned} \tag{13}$$

$$\Lambda_{kl} \equiv C^c_{kmln}n_{mn}, \quad n_{mn} \equiv n_m n_n, \quad n_1 = \frac{1}{a_1}\sin\theta\cos\varphi,$$

$$n_2 = \frac{1}{a_2}\sin\theta\sin\varphi, \quad n_3 = \frac{1}{a_3}\cos\theta.$$

Here, a_1, a_2 and a_3 are the semi-axes of ellipsoids modelling the mineral grains or cracks ($a_1 = a_2$). The derivation of this tensor can be found in the works of Shermergor (1977), Willis (1977), Kinoshita & Mura (1971) and Mura (1991). It can be shown that this tensor can be represented via the well-known Eshelby tensor $\mathbf{T}$ (1957) as follows

$$\mathbf{g} = -\mathbf{C}^{-\mathbf{1}}\mathbf{T}, \tag{14}$$

and relation (12) can be derived with the help of the Eshelby method under the assumption that the strain field of each inclusion is not affected by other inclusions (Bayuk *et al*. 2007). This corresponds to multiplication of the second derivative of the Green's function by the delta function in (11).

We assume that the inclusions differ in their elastic properties, shape and orientation in space. Let the rock under study contain N components (inclusion types) having different stiffness tensors $\mathbf{C_i}(i = 1, \ldots, N)$, and the volume concentration of each component is v_i. In the EMT it is assumed that the volume average can be replaced by the statistical average. Therefore, we can use the statistical distribution functions of inclusion volume over the parameters. We assume that the shape and orientation of inclusions of each type is described by the distribution function $P_i(\chi_i; \theta, \varphi, \psi)$; where χ_i is the AR of the *i*th inclusion type, and θ, φ, ψ are the Eulerian angles describing the inclusion orientation. If we average over all these parameters in (12), this formula can be written in the form

$$\begin{aligned}\mathbf{C}^* = &\left\{\sum_i v_i\mathbf{C_i}\int P_i(\chi_i;\theta,\varphi,\psi)\left[\mathbf{I} - \mathbf{g_i}(\mathbf{C_i} - \mathbf{C^c})\right]^{-1}\right. \\ &\times\sin\theta d\chi_i\mathrm{d}\theta\mathrm{d}\varphi\mathrm{d}\psi\Big\}\Big\{\sum_i v_i\int P_i(\chi_i;\theta,\varphi,\psi) \\ &\left.\times\left[\mathbf{I} - \mathbf{g_i}(\mathbf{C_i} - \mathbf{C^c})\right]^{-1}\sin\theta\mathrm{d}\chi_i\mathrm{d}\theta\mathrm{d}\varphi\mathrm{d}\psi\right\}^{-1}.\end{aligned} \tag{15}$$

In deriving the GSA method formula, the stiffness tensor of the comparison body is assumed to be arbitrary. The choice $\mathbf{C}^c = \mathbf{C}^*$ gives the formulas of the classical self-consistent method (Willis 1977). If we use the stiffest component as the comparison body, formula (15) gives the upper Hashin–Shtrikman bound; if the comparison body is the softest component, formula (15) provides the lower Hashin–Shtrikman bound (Ponte Castaneda & Willis 1995). A porous-cracked rock can be considered as a two-phase medium with the mineral matrix being the stiffest component and fluid as the

softest component. Applying the GSA method to the porous-cracked rocks, we take the comparison body in the form of a linear combination of the matrix (*m*) and fluid (*fl*) stiffness tensors: $\mathbf{C}^c = (1-f)\,\mathbf{C}^{(\mathbf{m})} + f\,\mathbf{C}^{(fl)}$. In this case, the choice $f = 0$ gives the upper Hashin–Shtrikman bound related to isolated fluid inclusions. The other limiting choice, $f = 1$, produces the lower Hashin–Shtrikman bound corresponding to the case when fluid forms a single-connected domain, and mineral grains are isolated. All intermediate structures are within these bounds. In this linear combination the factor f can be considered as a measure of the pore/crack connectivity. In what follows, this parameter is called friability. Note that the term 'friability' is used in geology in another meaning. Here, this parameter is only an empirical factor in the formula for the comparison body shown above.

We choose the GSA method for the inverse problem solution due to the fact that, among many theoretical methods, this method allowed us to obtain the closest fit of experimental and theoretical velocities for medium with known pore/crack geometry (Bayuk & Chesnokov 1998).

The functional to be minimized has the form

$$\Psi\left(\phi_{\rm ker}, \alpha_{\rm gc}, \theta, f, \phi_{\rm vert}, \alpha_{\rm vert}\right) = \sum_{i=1}^{N}\left[\frac{V_e^* - V_t^*(\phi_{\rm ker}, \alpha_{\rm gc}, \theta, f, \phi_{\rm vert}, \alpha_{\rm vert})}{V_e^*}\right]^2, \quad (16)$$

with the unknowns being the kerogen volume ($\phi_{\rm ker}$), AR of grain-related pore/cracks ($\alpha_{\rm gc}$), 'Gaussian sigma' (θ), friability (f), the volume concentration of the vertical cracks ($\phi_{\rm vert}$) and AR of vertical cracks ($\alpha_{\rm vert}$). Porosity plays a significant role in calculating the effective elasticity tensor. Therefore, we correct it within 2 per cent from the logging porosity and also include in the list of the unknown parameters. The 2 per cent is the value often reported as uncertainty in the logging porosity measurements (Ryjkov personal communication, 2003).

In formula (16), $N = 3$, since we have only V_P, V_{S1} and V_{S2} measured along a wellbore, but the number of unknowns is greater than the number of experimental points, which enhances non-uniqueness of the solution. In order to overcome this difficulty, we use optimization with bounds imposed on the unknown parameters. The bounds are as follows. The kerogen volume is limited from above by its amount derived from the core sample analysis, the grain-related aspect ratio varies from 1e-5 to 1, the standard deviation characterizing the platelet and pore/cracks orientation ranges from 0 to 90°, the volume concentration of vertical cracks changes from 0 to 1 per cent, the aspect ratio of vertical cracks varies from 1e-5 to 1e-2 and friability ranges from 0 to 1. The elastic moduli of fluid filling the pore space are supposed to be known. Additional conditions used in the optimization are (1) the shear wave splitting calculated from the theoretical velocities should not differ from the experimental one more than 2 per cent and (2) the Thomsen parameters ε and γ found for shale without vertical cracks do not exceed 0.6, which is in correspondence with experimental data (Vernik & Liu 1997; Li 2006). The splitting is calculated as the difference between the fast and slow V_S divided by their average value and multiplied by 100 per cent.

The non-linear optimization is carried out with the help of the direct search complex algorithm included in the library of Compaq Visual Fortran 6.6.

Note that the elastic properties of clay '*in situ*' are different from the properties of clay monocrystals due to the ability of clay to adsorb water. The elastic moduli of the bound water differ from those of the bulk water, since the bound water forms ordered structures. This results in the fact that the shear modulus of the bound water can be nonzero (Sayers 2005). The amount of the adsorbed water depends on the clay type. Katahara (1996) estimated that water adsorbed by smectite can occupy around 20 per cent of its volume, whereas this value for illite is only around 4 per cent. This depends on the clay platelet thickness. In this work, shales consisting mostly of illite are considered. To date, no published data on the stiffness tensor of an '*in situ*' illite-rich clay exist. Wang *et al*. (2001) reported the bulk and shear moduli of '*in situ*' illite aggregate found with the help of EMT from measurements of elastic properties of artificial samples made from illite platelets mixed with epoxy resin. When preparing the sample, they kept the bound water adsorbed by the illite platelets. Their estimation of the bulk and shear moduli of the '*in situ*' illite polycrystal are $K = 60.1$ and $\mu = 25.3$ GPa, respectively. Note that Katahara (1996) reported the Voigt–Reuss–Hill average for an illite polycrystal formed by pure illite monocrystals (without bound water) as $K = 55.5$ and $\mu = 31.8$ GPa. The stiffness tensor of illite monocrystal was taken from the work of Alexandrov & Ryzhova (1961). As seen, the bound water lowers the illite shear modulus by 22 per cent. The difference in bulk modulus is around 7 per cent and can be neglected due to the experimental errors and errors provided by the theoretical approaches used.

In this work, we estimate the stiffness tensor of '*in situ*' illite as follows. We assume that the illite monocrystals incorporate thin layers of bound water, and the aspect ratio of bound-water layers is the same as that of the clay platelets, that is, 1e-5. We include the bulk and shear moduli of the bound water in the list of the parameters to be found (in addition to the unknown parameters of the shale model mentioned above) and assume that the moduli of the bound water are no less than those of pure water but smaller than those of kerogen. The bulk and shear moduli of kerogen are taken as $K = 7.0$ and 3.2 GPa, respectively, with the density of 1.25 g cm^{-3} (Vernik & Liu 1997). Applying the optimization, we fit the friability of the bound water and volume of the bound water such that the bulk and shear moduli of 'in situ' illite should be close to those reported by Wang *et al*. (2001). We apply the optimization to selected depth intervals of the wellbore under study and find that if the bound-water friability equals 0.98, and the bound water occupies 2 per cent of illite volume, the bulk and shear moduli of the stiffness tensor of '*in situ*' illite varies around 57.6 and 27.2 GPa, which is very close to the Wang results. The components of stiffness tensor of the '*in situ*' illite providing these moduli are (in the Voigt notation): $C_{11} = 127.4$, $C_{33} = 54.7$, $C_{44} = 14.4$, $C_{66} = 39.7$ and $C_{13} = 28.4$ (in GPa). The bound-water moduli found in such a way for the selected depth intervals averages 6.8 and 0.04 GPa, respectively, with the standard deviation 1.5 and 0.04 GPa. Note that these moduli of bound water are found for the fixed friability (0.98) and bound-water content (2 per cent from the illite volume). An increase in friability leads to increase in the bound-water shear moduli, but the bulk modulus remains rather stable. Thus, for friability 0.999 and 4 per cent of bound water in clay content, we obtain the bulk and shear moduli of bound water 6.7 and 0.24 GPa, respectively.

2.3 Analysis of inversion stability with respect to the shale's stiffness tensor

Since the shale's stiffness tensor is reconstructed only from measurements in the vertical direction, that is, we have direct information only on C_{33}, C_{44} and C_{55}, the question arises of stability of the other components found from the inversion.

First, we consider a shale of VTI symmetry (without vertical cracks) and analyse the stability of C_{11}, C_{13} and C_{66} inverted from the V_P and V_S measured in the vertical direction. In our modelling we assume that this direction is normal to the bedding. In this case, the fast and slow S waves have the same velocities in this direction. We analyse stability of the stiffness tensor components provided by the inversion as follows. The forward problem is solved for given mineral composition of shale and porosity but for varying friability, aspect ratio of grain-related pore/cracks and angle of orientation of clay platelets and grain-related pore/cracks. The grain-related pore/cracks are assumed to be water-saturated. The friability varies from 0 to 0.99, the aspect ratio changes from 1e-5 to1 and the angle ranges from 0 to 90°. As a result a set of stiffness tensors is obtained.

Then, for each pair of C_{33} and C_{44} values (corresponding to V_P and V_S propagating in the vertical direction) possible variations in C_{11}, C_{66} and C_{13} are analysed. In this analysis, it is assumed that C_{33} and C_{44} vary within a given range comparable with experimental error. Note that the variation in the respective velocities is two times smaller.

This analysis is carried out for Greenhorn shale (Jones & Wang 1981) for which both the mineral compositions and the stiffness tensor are well known. The clay in Greenhorn shale is not composed by illite only. The clay consists of almost equal amounts of illite and smectite (36 per cent and 34 per cent) and almost equal amounts of kaolinite and chlorite (17 per cent and 13 per cent). The total clay content is around 30 per cent. The '*in situ*' stiffness tensor of such a clay was inverted from the laboratory measurements of Jones & Wang (1981) by Bayuk *et al*. (2007). We select only the solutions for which the Thomsen parameters ε and γ no more than 0.6. To analyse the stability of C_{11}, C_{66} and C_{13}, we use the standard deviation normalized by the average value

$$\sigma_{ij}^{N} = \frac{\left(\sqrt{\frac{(C_{ij}-C_{ij\_aver})^2}{N}}\right)}{C_{ij\_aver}} \times 100, \qquad (17)$$

where N is the number of solutions for the given C_{33} and C_{44} range and C_{ij_aver} is the average value of the respective C_{ij} over the N solutions. The normalized standard deviation (NSD) for C_{11}, C_{13} and C_{66} inverted for shales of composition similar to the Greenhorn shale is shown in Fig. 2. In this analysis we assume that C_{33} and C_{44} vary within 2 per cent (error level in the laboratory measurements). As seen, the NSD does not exceed 13, 9 and 22 per cent for C_{11}, C_{13} and C_{66}, respectively. The average values of the NSD for C_{11}, C_{13} and C_{66} are, respectively, 5, 3 and 9 per cent. The maximum standard deviation is observed for the component without index '3', that is, for C_{66}. If we consider greater uncertainties in V_P and V_S propagating in the vertical direction, for example, 3 and 5 per cent, which corresponds to the experimental errors in logging data, the respective average values of NSD are 7, 6 and 11 per cent.

Now we insert the vertical cracks in the shale and analyse the stability of the stiffness tensor inversion if splitting is observed in the logging data. The symmetry axis of the vertical cracks is assumed to be parallel to the Y-axis (with Z being the vertical axis). Fig. 3 demonstrates a change in the stiffness tensor components with volume concentration of vertical cracks of aspect ratio 0.005 at friability 0.78. The vertical cracks are assumed to be water-saturated. As seen, among the three components derived from logging (C_{33}, C_{44} and C_{55}) the vertical cracks affect only C_{44}. This means that analysing the difference between C_{44} and C_{55}, we can reconstruct the shape of vertical cracks. In our model, the friability is assumed to be the same for grain-related pore/cracks and vertical cracks.

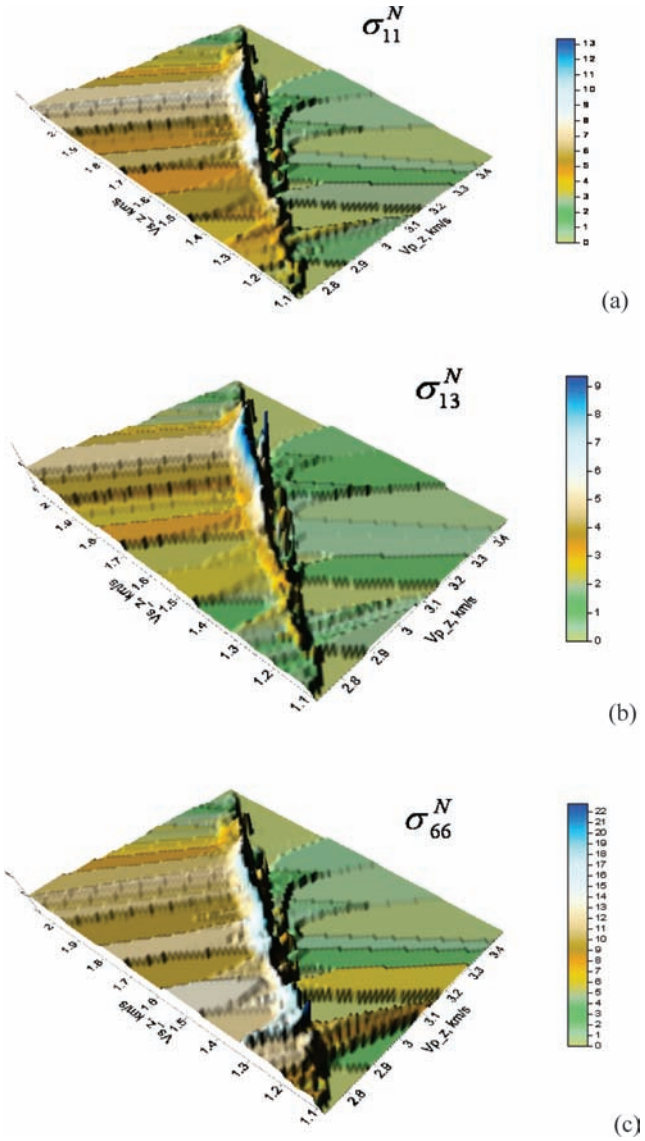

Figure 2. Normalized standard deviation for (a) C_{11}, (b) C_{13} and (c) C_{66} inverted from the V_P and V_S measured in vertical direction with uncertainty ±1 per cent.

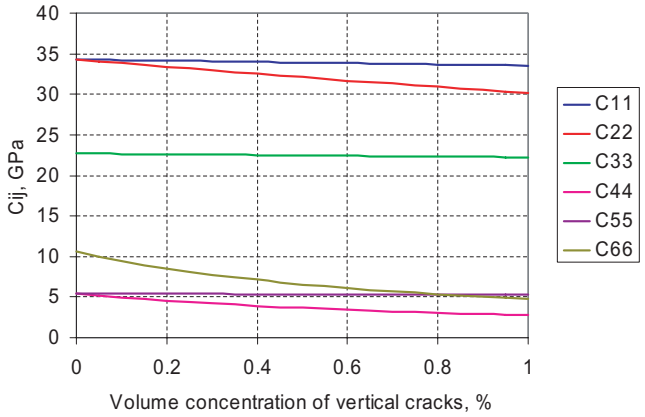

Figure 3. Effect of vertical cracks (aspect ratio 0.005) on the components of shale's stiffness tensor.

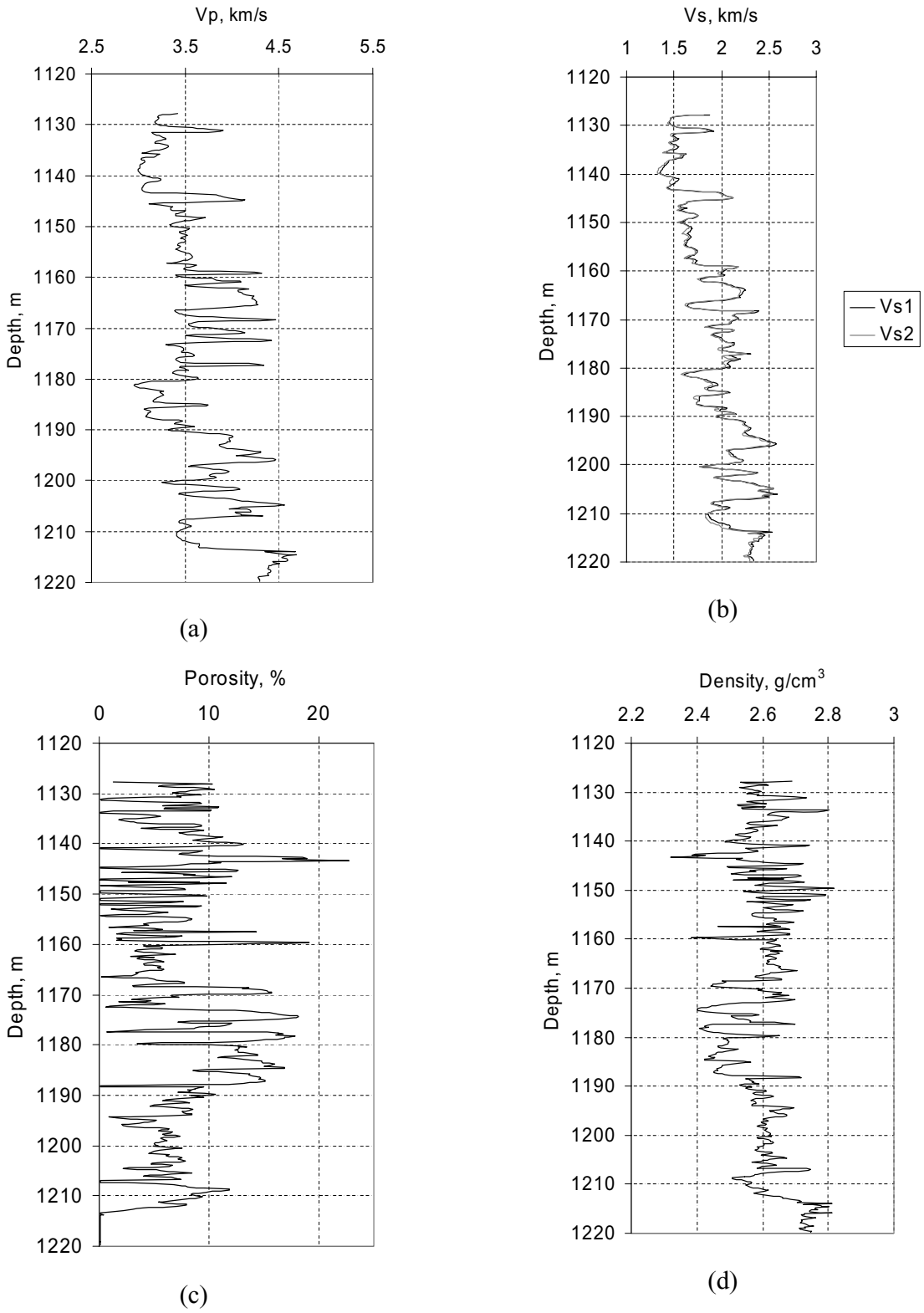

Figure 4. Initial logging data used for inversion of shale's stiffness tensor. (a) V_P, (b) fast and slow V_S, (c) porosity (density porosity), (d) density, (e) content of silt minerals, (f) water saturation of pore/crack space. The notation 'Qz', 'Lms' and 'Dol' means quartz, limestone and dolomite.

After the shape of vertical cracks is found, all components of the resulting stiffness tensor having the orthorhombic symmetry are calculated with the help of GSA method. According to our analysis, the uncertainty in the components C_{22}, C_{23} and C_{12} is comparable with the uncertainty in C_{44}.

2.4 Choice of the solution to the shale's stiffness tensor

The direct complex search algorithm is applied (Subprogram DBCPOL of the Compaq 6.6 Fortran library) for the optimization. At each step of this algorithm a polygon having $2n$ vertices is

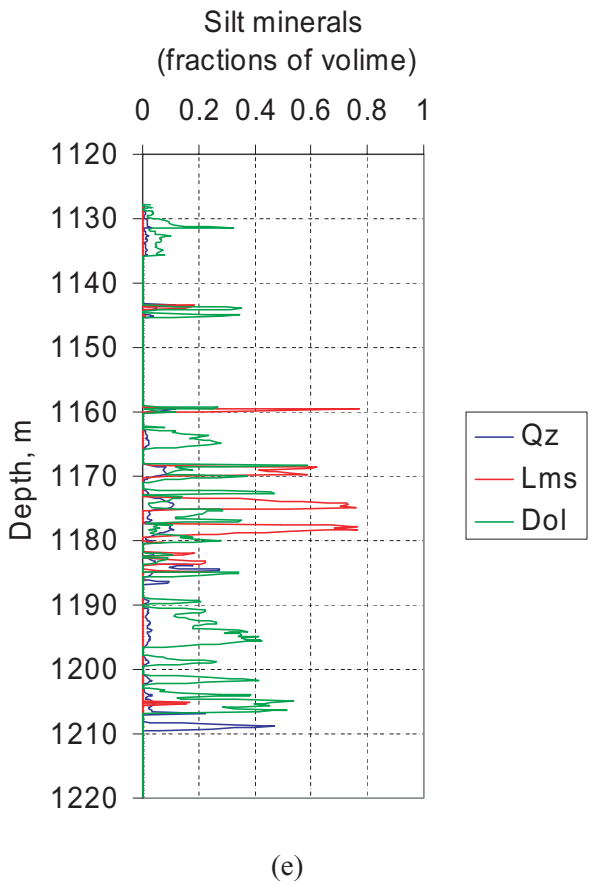

(e)

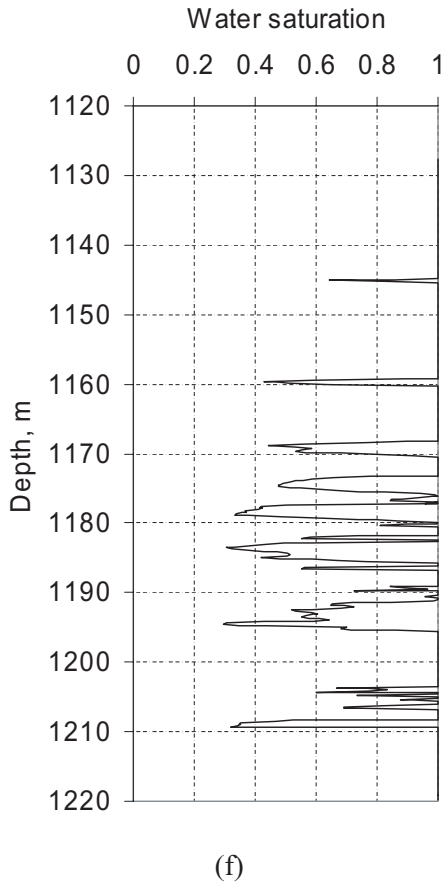

(f)

Figure 4. *(Continued.)*

considered (n is the number of unknowns). The vertex at which the function has the maximum values (among $2n$ vertices) is replaced by a point with better value of the function. The process terminates when all points of the polygon are close to minimum. The condition of closeness to minimum is selected by the user. It makes sense to stop the process when the algorithm stably produces the misfit between the experimental and theoretical values of velocities comparable or somewhat less than the experimental errors. Note that in this algorithm, the minimized function does not gradually decrease with the number of iterations. Even in the beginning of the process acceptable values of the function can be obtained.

Since the experimental velocities used in the optimization are not exact values but contain experimental errors, the absolute minimum of the function minimized may not produce actual values of the unknown parameters. In order not to loose the actual solution, we collect all the solutions in the optimization process, which provide an acceptable misfit between experimental and theoretical velocities. This also gives an opportunity to analyse the stability of the parameters found. We analyse the variability in the stiffness tensor components provided by the acceptable solutions for Greenhorn shale in the both dry and water-saturated state. For the dry sample we calculate the shale's stiffness tensor theoretically using the microstructure inverted from the Jones & Wang (1981) measurements on the saturated sample. It was found that the stiffness tensor components in the set of suitable solutions are rather stable varying within 6 per cent for the diagonal components and within 12 per cent for C_{13}. This gives us an opportunity to take a solution to every component of the shale's stiffness tensor as the average value of all suitable solutions.

2.5 Results of the shale's stiffness tensor reconstruction

The aforementioned optimization technique is used to solve the upscaling problem for a wellbore for which all logging data necessary for the inversion are available. The initial logging data are shown in Fig. 4. Note that the shear wave splitting attains 6 per cent for this well. The clay content in the shale equals unity minus the sum of the volume fractions of silt-sized minerals and varies from 10 per cent to almost 100 per cent. We accept the solutions providing a misfit between experimental and theoretical velocities no more than 3 and 5 per cent for V_P and V_S, respectively. One of the solutions to the parameters of shale's microstructure found from the inversion is shown in Fig. 5. The kerogen content for samples extracted from this well is no more than 15 per cent. We use this value as the upper bound for the kerogen content. The set of the following three parameters: AR of grain-related voids, friability and Gaussian sigma are responsible for the anisotropy of shale without vertical cracks (VTI anisotropy). Small values of AR and Gaussian sigma result in enhanced anisotropy. Theoretical modelling with the GSA method shows that different values of friability produce different anisotropy whereas the other model parameters are fixed. Vernik & Liu (1997) reported that the shale anisotropy in kerogen-rich shales is also affected by kergen content. However it depends on that if kerogen forms a continuous matrix or exists in the form of isolated non-isometric inclusions.

As was shown above, many sets of the parameters produce similar values of the shale's stiffness tensor. Fig. 5 demonstrates one possible set of the parameters. In order to find the parameters with less uncertainty, additional information is needed. For example, narrower

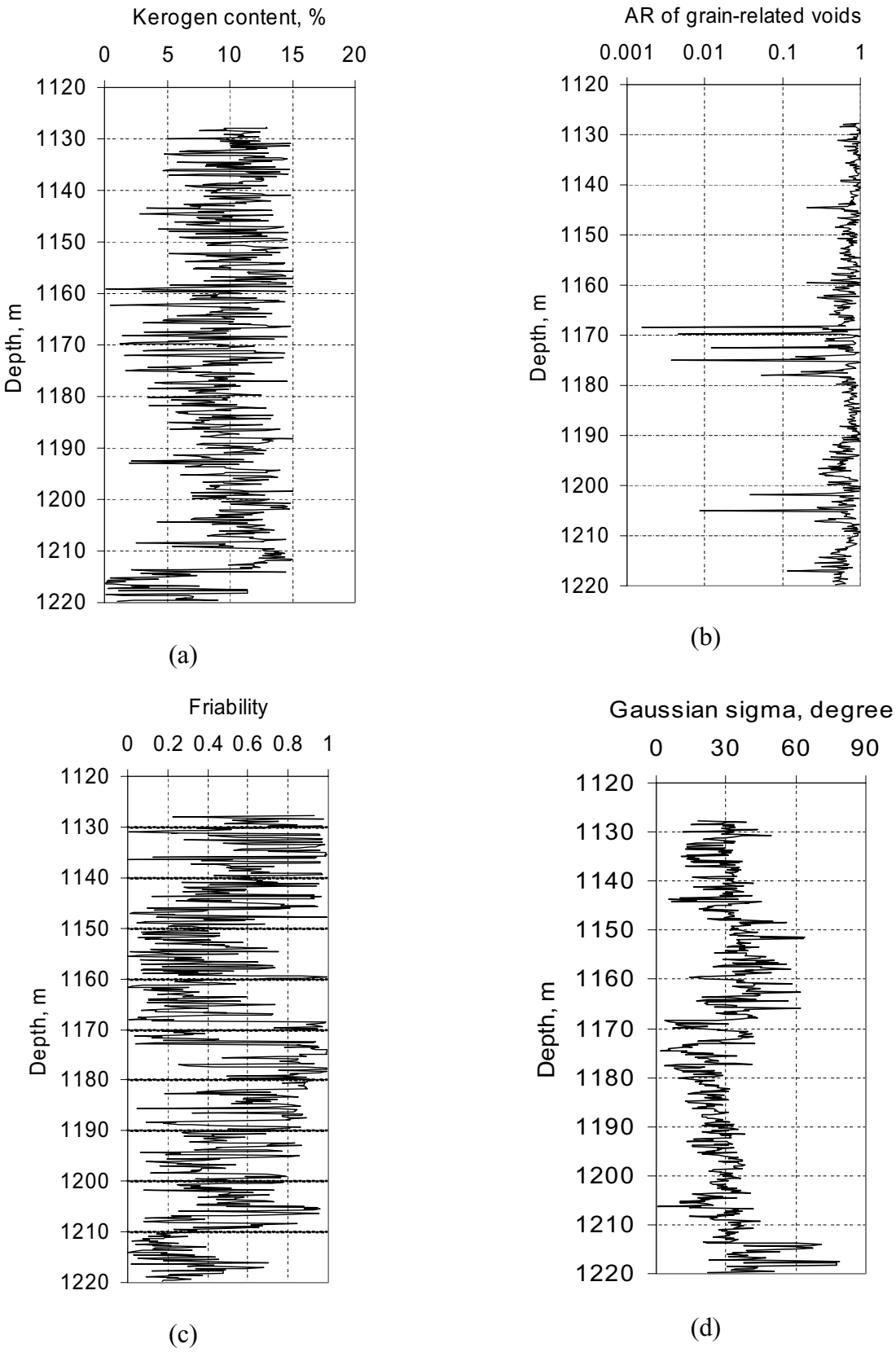

Figure 5. Parameters of shale microstructire found from the inversion: (a) kerogen content, (b) AR of grain-related voids, (c) friability, (d) Gaussian sigma, (e) amount of vertical cracks and (f) AR of vertical cracks.

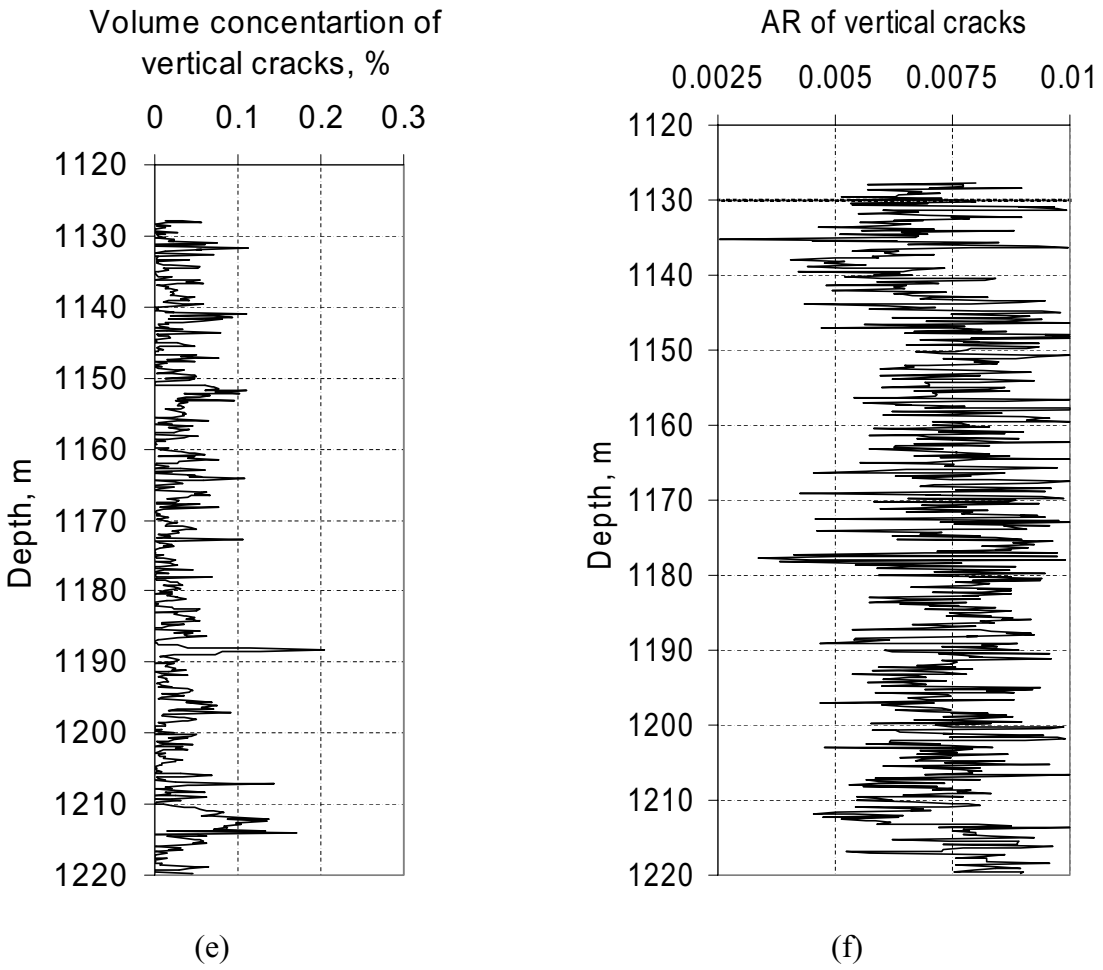

Figure 5. *(Continued.)*

bounds for the Gaussian sigma can be derived from thin section analysis. The same is valid for the vertical cracks. One and the same splitting can be derived at different pairs of volume concentration of vertical cracks and their AR.

The components of the shale's stiffness tensor found from the inversion are shown in Figs 6(a)–(c). The relative difference between the respective components responsible for the difference between VTI symmetry and orthorhombic symmetry is shown in Fig. 6(d). As seen, the inverted stiffness tensor can be considered as having orthorhombic symmetry, since the difference between the components C_{44} and C_{55} attains 13 per cent. This means that the maximum difference in the respective velocities is around 6.5 per cent, which is greater than the experimental errors of the shear wave splitting in the dipole sonic measurements (Ryjkov personal communication, 2003). The Thomsen parameters calculated for the shale without vertical cracks, that is, for VTI medium are shown in Fig. 7. As seen, ε and γ varies from 0 to 0.6 averaging 0.22 and 0.32, respectively. The Thomsen parameter δ ranges from –0.5 to 0.3 and has the average value equal to 0.09. As seen, δ is positive for all depths where 100 per cent water-saturation is indicated. For these depths, the grain-related voids are rather isometric: their aspect ratio is greater 0.1 (Fig. 4b), which can be explained by the fact that thin cracks are closed '*in situ*' due to the pressure effect. Note that mostly positive values of δ were observed by Vernik & Liu (1997) for brine-saturated shales in laboratory experiment at 70 MPa confining pressure. Based on the Hudson theory (1981) which predicts negative δ for fluid-saturated rocks containing thin cracks, they attributed the positive sign of δ to closure of thin cracks under elevated pressure. Note that negative values of δ inverted from logging data may indicate zones of enhanced pore pressure which prevents closure of thin cracks.

3 SOLUTION OF UPSCALING PROBLEM FOR LAYERED MEDIUM

We consider a wave propagating in a layered medium whose layers have orthorhombic symmetry. In order to calculate the stiffness tensor at given frequency lower than sonic frequency at given depth, the depth is set to be the centre of layered medium whose layers have pore/crack geometry, friability and stiffness tensor of mineral matrix found at the first step. The layer thickness equals the step of sonic logging, and the number of layers is such that the layers cover the depth interval equal to the wavelength (Bayuk *et al*. 2003a). Thereby the number of layers at each depth depends on the given frequency. The running window method is applied to obtain the elasticity tensor versus depth at given frequency (for example, seismic frequency).

3.1 Method for the upscaling problem solution

We assume that the horizontal symmetry axes of each layer are directed along the X and Y-axes of laboratory coordinate system

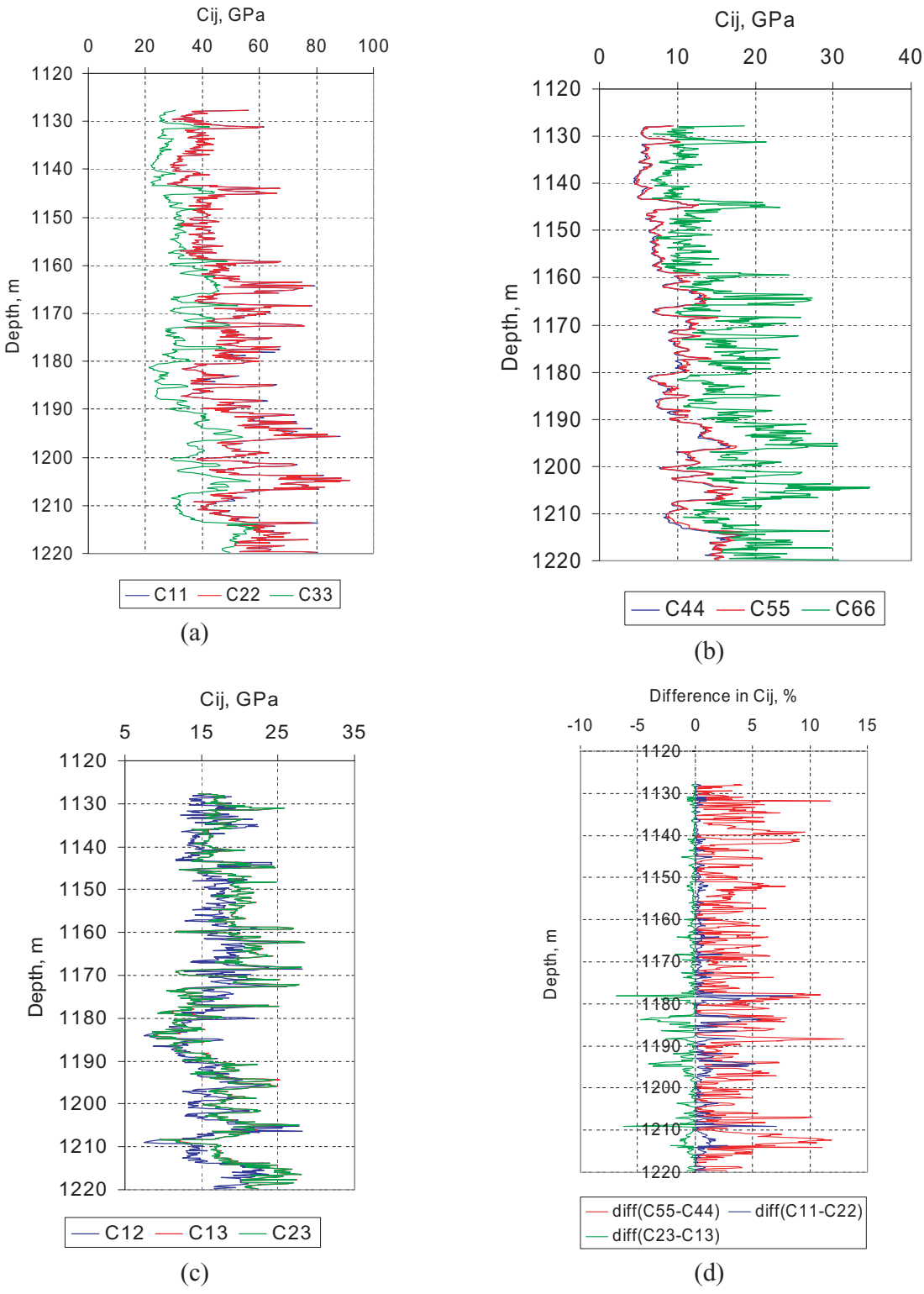

Figure 6. (a)–(c): components of shale's stiffness tensor found from the inversion and (d) their relative difference.

whose Z-axis is directed upward. As a rule, the crack azimuth derived from sonic logging is almost constant or slightly varies along a wellbore, therefore, this assumption is acceptable for upscaling of logging data. If the layer thickness is small enough compared to the wavelength, the exact solution for the effective stiffness tensor of the layered medium is calculated by the formulas (Shermergor 1977) whose derivation is given in Appendix:

$$C_{11}^{*} = \langle C_{11} \rangle + \left\langle \frac{C_{13}}{C_{33}} \right\rangle^{2} \langle C_{33}^{-1} \rangle^{-1} - \left\langle \frac{C_{13}^{2}}{C_{33}} \right\rangle,$$

$$C_{12}^{*} = \langle C_{12} \rangle + \left\langle \frac{C_{13}}{C_{33}} \right\rangle \left\langle \frac{C_{23}}{C_{33}} \right\rangle \langle C_{33}^{-1} \rangle^{-1} - \left\langle \frac{C_{13} C_{23}}{C_{33}} \right\rangle,$$

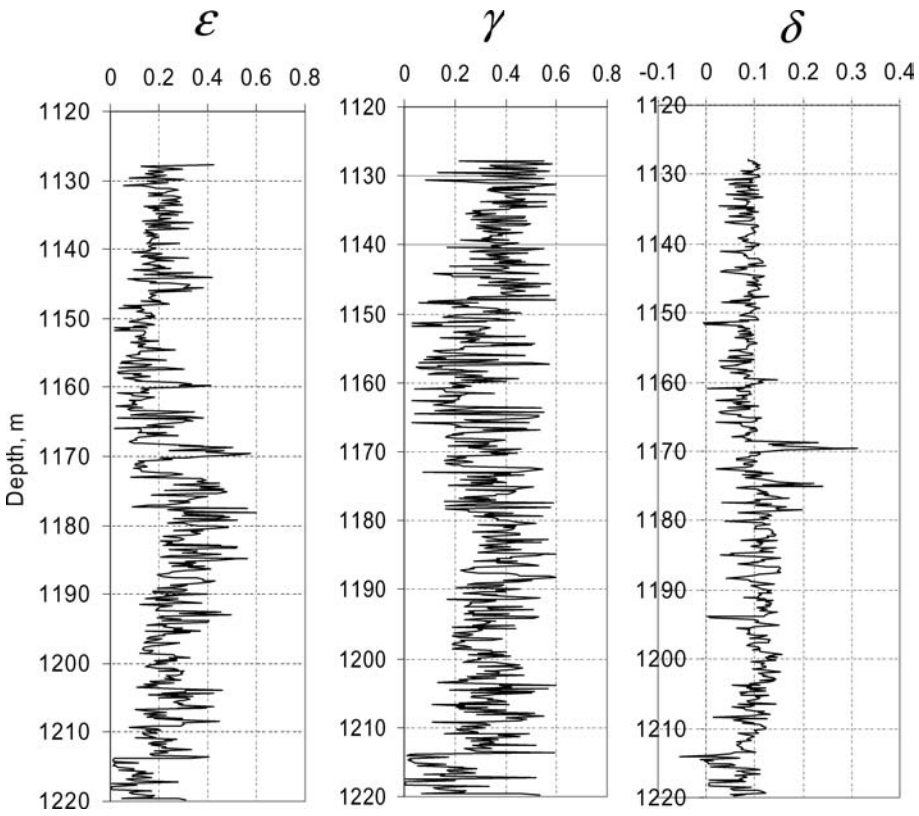

Figure 7. The Thomsen parameters of the shale (VTI symmetry) without the vertical cracks.

$$C_{13}^{*} = \left\langle \frac{C_{13}}{C_{33}} \right\rangle \left\langle C_{33}^{-1} \right\rangle^{-1},$$

$$C_{22}^{*} = \langle C_{22} \rangle + \left\langle \frac{C_{23}}{C_{33}} \right\rangle^{2} \left\langle C_{33}^{-1} \right\rangle^{-1} - \left\langle \frac{C_{23}^{2}}{C_{33}} \right\rangle,$$

$$C_{23}^{*} = \left\langle \frac{C_{23}}{C_{33}} \right\rangle \left\langle C_{33}^{-1} \right\rangle^{-1}, \; C_{33}^{*} = \left\langle C_{33}^{-1} \right\rangle^{-1},$$

$$C_{44}^{*} = \left\langle C_{44}^{-1} \right\rangle^{-1}, \; C_{55}^{*} = \left\langle C_{55}^{-1} \right\rangle^{-1}, \; C_{66}^{*} = \langle C_{66} \rangle \qquad (18)$$

As seen, these formulas are applicable for layers having orthorhombic symmetry. If all layers are isotropic, the formulas are reduced to those derived by Backus (1962) and Rytov (1956) for a fine-layered medium, and resulting medium exhibits transversely isotropic type of symmetry with the vertical axis of symmetry (i.e. VTI). Formula (18) can be considered as a generalization of the Backus approach, widely used for upscaling, to the case of anisotropic (orthotropic) layers.

When calculating by formula (18), the averaging is carried out using a moving window whose size is equal to wavelength at the depth which is at the centre of the window. The aforementioned method is applicable for the logging data we have, since the layer thickness, 0.5 ft (or 15 cm), is several times smaller than the wavelengths of *P* and *S* waves being on average, respectively, 10 and 5 m for 500 Hz (the smallest wavelength when considering the frequency interval 100–500 Hz for which the upscaling is performed).

Formula (18) allow us to estimate uncertainty in the upscaled components from the uncertainties found at the sonic frequency. Our estimations for shales having composition similar to Greenhorn shale give that if we accept the errors in V_P and V_S velocities as 3 and 5 per cent, the averaged values of NSD for the components of upscaled tensor are as follows: 14 per cent for C_{11}, C_{22} and C_{12}; 10 per cent for C_{13} and C_{23}, 11 per cent for C_{66}; 6 per cent for C_{33}; 10 per cent for C_{44} and C_{55}. Note that the NSD in the elastic wave velocities propagating in the principal directions are two times smaller than that for the respective C_{ii}. This means that the averaged NSD for *Vp*(11), *Vp*(22) and *Vp*(33) are, respectively, 7, 7 and 3 per cent, and for *Vs*(44), *Vs*(55) and *Vs*(66) are, respectively, 5, 5 and 6 per cent. Here, in parentheses, the indices for the respective component of the stiffness tensor are shown. Note that these uncertainties are dependent on the shale composition, and our estimations performed for the Greenhorn shale provide only an idea of how great the uncertainties could be. However, the estimations performed for an illite-rich shale (illite occupies 80 per cent of shale volume) give similar results. Note also that the NSD values presented here are an average over a set of solutions obtained for different microstructure parameters. For each particular case of the shale microstructure, the NSD can be different. The maximum NSD estimated for the Greenhorn shale are 17 per cent for C_{11}, C_{12}, C_{22} and C_{66}; 13 per cent for C_{13}, C_{23}; 6 per cent for C_{33}; and 10 per cent for C_{44} and C_{55}.

3.2 Results of upscaling problem solution

Formulas (18) of the previous section are applied to a layered medium consisting of anisotropic layers of orthorhombic symmetry, the elastic properties of which are found from the inverse problem solution as discussed above. The results of upscaling for the diagonal components C_{11}, C_{33}, C_{44} and C_{66} of elasticity tensor at 500 Hz are shown in Fig. 8 in comparison with the components inverted at the sonic frequency. Fig. 9 shows all components of the stiffness tensor at 500 Hz. Fig. 10 demonstrates the anisotropy of elastic wave velocities calculated from the stiffness tensor at 500 Hz. The abbreviations '*xy*', '*xz*' and '*yz*' indicate the anisotropy of V_P in the respective planes. The symbols '44_55', '44_66' and '55_66'

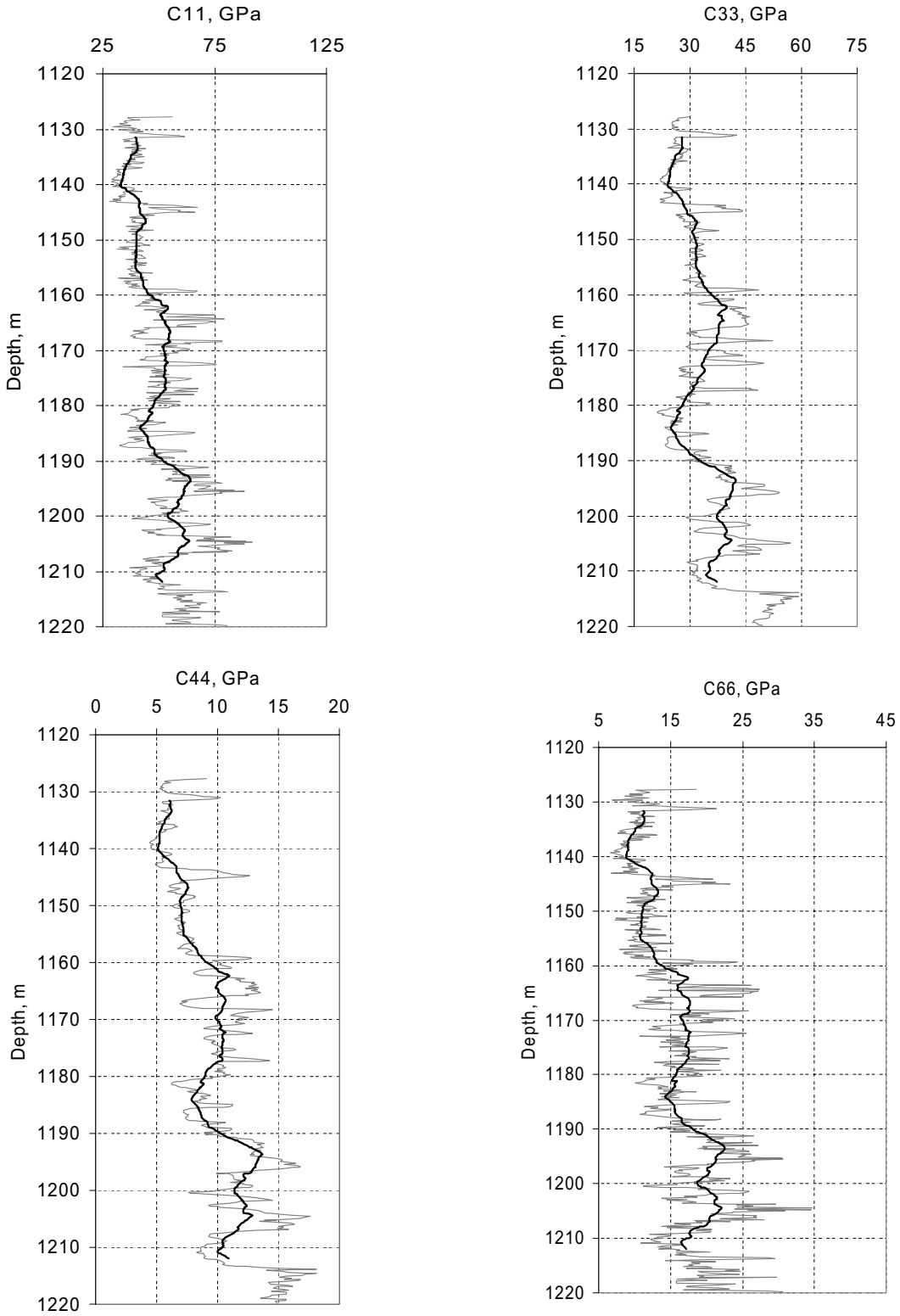

Figure 8. Comparison of the stiffness tensor components at sonic frequency and at 500 Hz. Grey curves are the components at the sonic frequency, and black curves are the components at 500 Hz.

indicate the anisotropy of shear wave velocities calculated for the respective C_{ii} ($i = 4$, 5 and 6). As seen, the anisotropy in the bedding plane is comparable with the experimental errors (Ap_xy $\approx$ 3 per cent and As_44_55 $\approx$ 5 per cent), and the shale can be considered as a transversely isotropic medium (VTI). The anisotropy coefficients vary from 0 to 27 per cent for V_P and from 1 to 32 per cent for V_S. The Thomsen parameters calculated for this shale from the upscaled stiffness tensor are shown in Fig. 11. As expected, the variations of the parameters with depth are smaller compared to the variations at

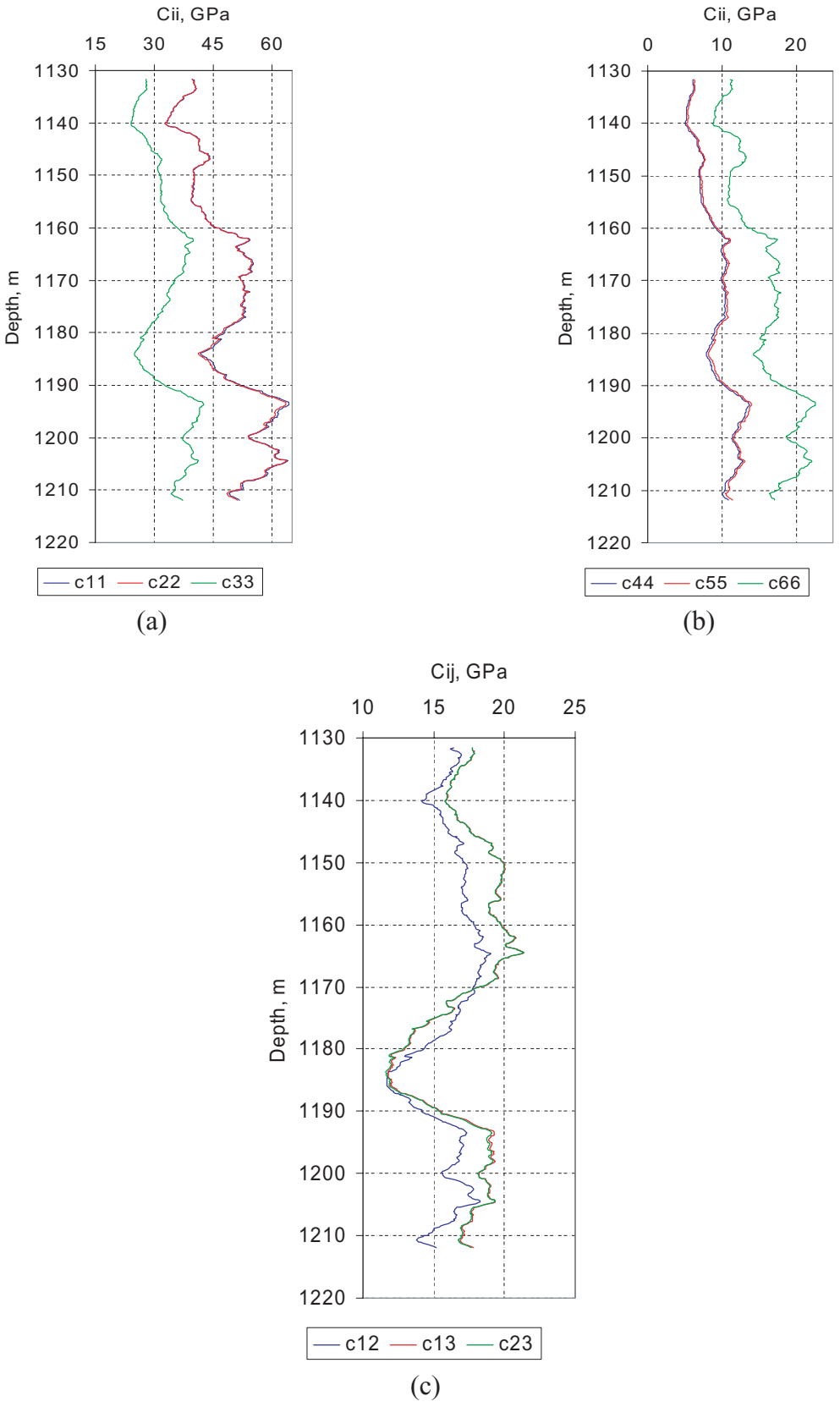

Figure 9. Components of the shale's stiffness tensor at 500 Hz: (a) the diagonal components C_{11}, C_{22}, and C_{33}; (b) the diagonal components C_{44}, C_{55} and C_{66}; and (c) off-diagonal components C_{12}, C_{13} and C_{23}.

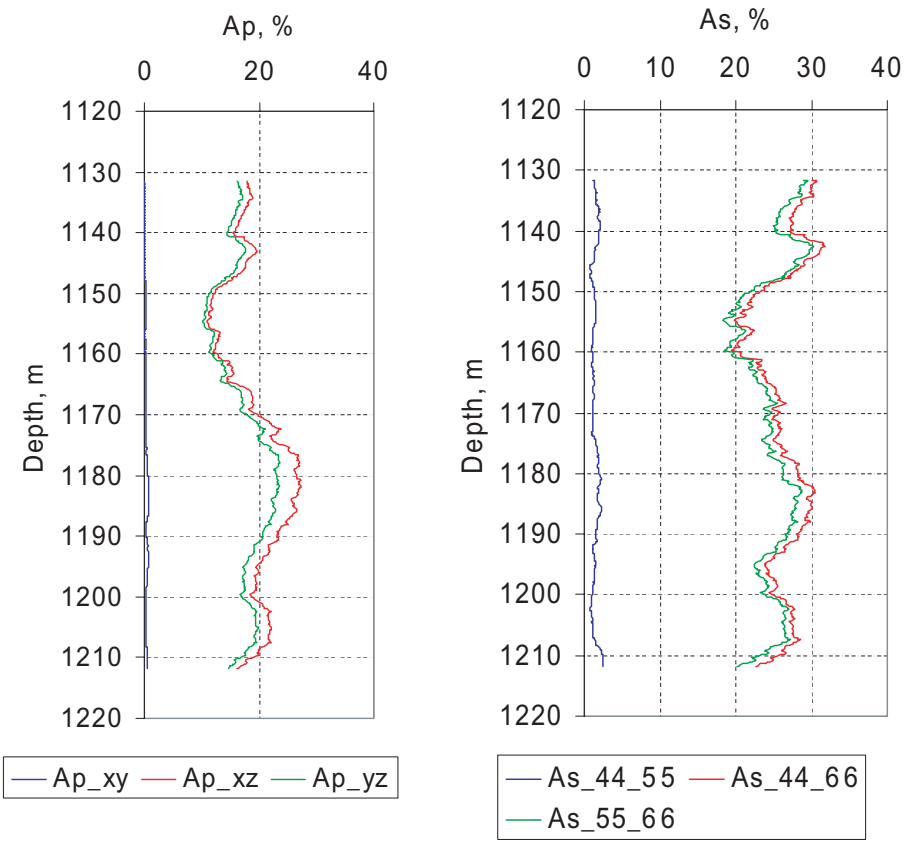

Figure 10. Velocity anisotropy of shale at 500 Hz. $A_x = \frac{V_{\max} - V_{\min}}{0.5(V_{\max} + V_{\min})} 100$ per cent.

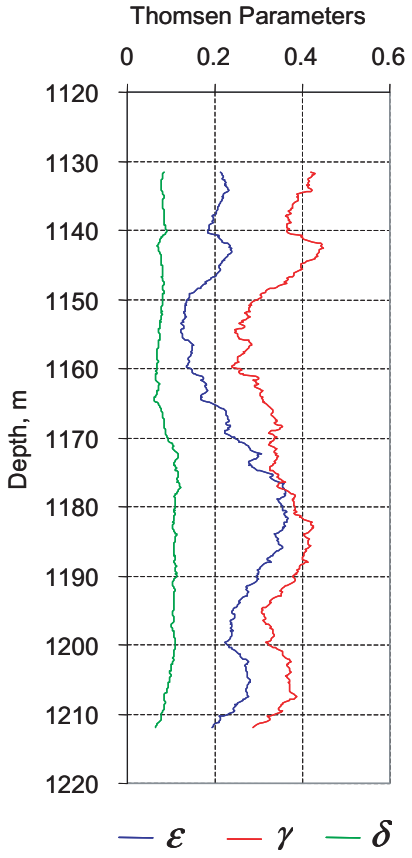

Figure 11. The Thomsen parameters of the shale found at 500 Hz.

the sonic frequency. The maximum values of ε and γ are 0.38 and 0.45, respectively.

We can conclude that the symmetry of shale stiffness tensor is different at different scale levels. The stiffness tensor of shale under study is of orthorhombic symmetry at sonic frequency and of VTI symmetry at 500 Hz. Note that this result is not common for all shales and is related to a specific shale. This shale is characterized by rather high clay content and low splitting of shear wave velocities attributed to vertical cracks. The symmetry at sonic and lower frequency depends on the clay content and amount of vertical cracks. If the clay content is considerable, the factors resulting in VTI symmetry exist. However, there is no strong correlation between the clay content and degree of anisotropy, because VTI anisotropy in shales is controlled by the following parameters: AR of grain-related pore/cracks, Gaussian sigma, friability and kerogen content. This leads to the recognition that at the same clay content, one may observe different anisotropy.

If the clay content is fixed, of interest are correlations between the Thomsen parameters (ε and γ) and shale's model parameters responsible for VTI anisotropy. For example, a negative correlation between the Thomsen parameters and Gaussian sigma is seen for shales having the clay content varying from 0.6 to 0.7 (Figs 12a and b). The correlation is stronger for ε than for γ. However, if the clay content is smaller and ranges from 0.25 to 0.4, this correlation is weak (Figs 12c and d). No distinct correlations are observed between the Thomsen parameters and other shale's model parameters that affect the shale's VTI anisotropy within these intervals of clay content. This means that it is impossible to reveal a principal parameter affecting the shale anisotropy in general case. The anisotropy observed is a combined effect of all the shale's model parameters mentioned above.

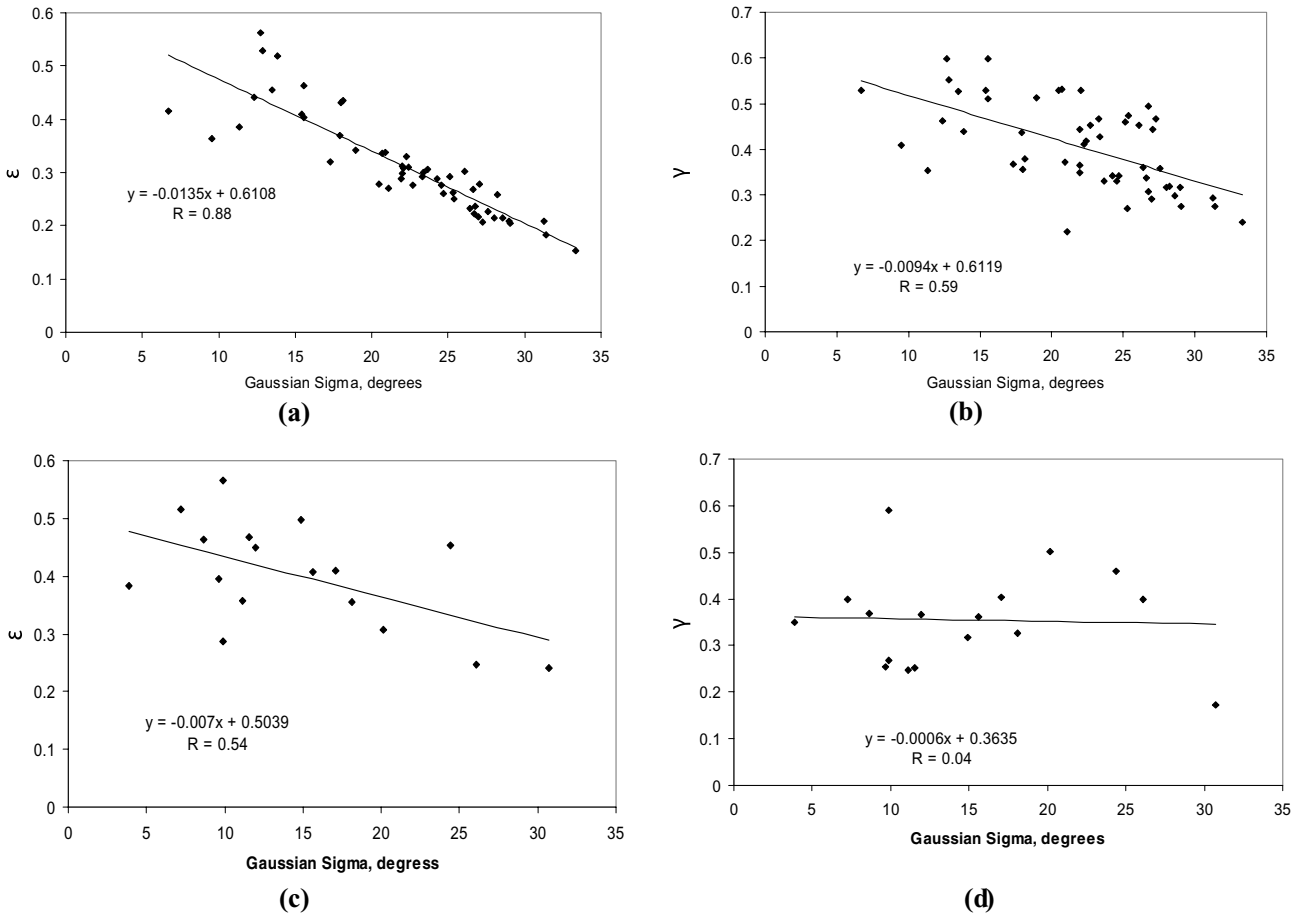

Figure 12. Correlation between the Thomsen parameters and Gaussian sigma for shales having different clay content: (a) and (b) clay content varies from 0.6 to 0.7; (c and d) clay content varies from 0.25 to 0.4. *R* is the correlation coefficient.

Enhanced amount of vertical cracks in VTI medium results in the orthorhombic symmetry, since the vertical cracks in isotropic medium cause HTI symmetry. The layering contributes to VTI symmetry; however, it depends on the contrast between the layers. The greater the contrast in elastic properties, the greater is the contribution. In order to demonstrate how the vertical cracks can change the stiffness tensor symmetry, we consider artificial shale with greater amount of vertical cracks producing splitting up to 22 per cent. The VTI stiffness tensor of this shale (without vertical cracks) is the same as that of natural shale for which the inversion has been performed. Analysis of the results shown in Fig. 13 allows us to observe how the symmetry of the shale's stiffness tensor found at 500 Hz changes from VTI to orthorhombic with increasing amount of vertical cracks. The numbers in notation indicate the amount of vertical cracks relative to that inverted from the original data. Thus, '1' means that the amount of vertical cracks used for the anisotropy analysis is exactly the same as inverted, '2' means that the volume concentration of vertical cracks is twice as high as that found from the inversion and '4' means that the volume concentration of vertical cracks used for the analysis is four times greater than that provided by the inversion.

4 CONCLUSIONS

A method for upscaling of elastic properties of shales has been proposed. The method includes the following two steps.

(1) The first step includes an inversion of the shale's microstructure parameters (pore/crack geometry, orientation of clay platelets and grain-related cracks relative the bedding plane, shape and amount of vertical cracks, pore/crack connectivity and kerogen content) from the logging data at sonic frequency. Using the parameters found, all components of the effective stiffness tensor are calculated for each logging depth. In the presence of vertical cracks, the symmetry of resulting tensor is orthorhombic.
(2) The second step assumes a calculation of the elasticity tensor of layered medium at lower frequency from tensors at sonic frequency found at the first step. The stiffness tensor symmetry of the resulting medium at lower frequency is dependent on the microstructure parameters and can be hexagonal or orthorhombic.

All of the microstructural parameters mentioned above together with the clay content contribute to the shale's anisotropy and its type (VTI or orthorhombic) at the scale of sonic measurements. Different combinations of these parameters may produce the same anisotropy in the elastic properties of shales, and it is very difficult to reveal the main parameter affecting shale anisotropy in general.

The elastic properties of the shale under study are characterized by orthorhombic symmetry at the scale of sonic measurements. The Thomsen parameters characterizing the anisotropy of VTI shale (without vertical cracks) at sonic frequency vary from 0 to 0.6 for ε and γ and from –0.5 to 0.3 for δ. The average values of the parameters are 0.22, 0.32 and 0.09, respectively, for ε, γ and δ. At the

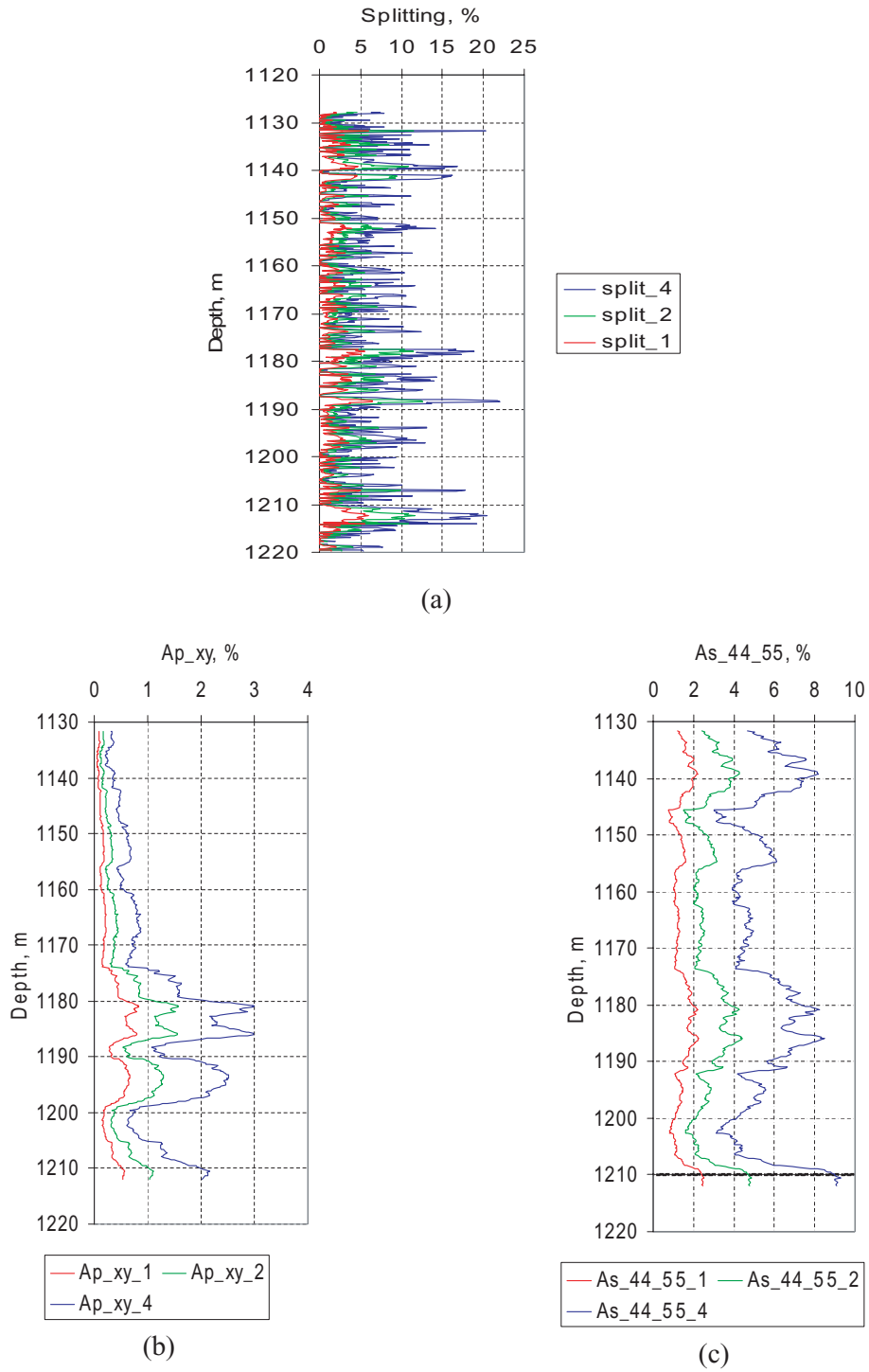

Figure 13. Shear wave splitting at the sonic frequency and anisotropy of elastic wave velocities at 500 Hz for different amount of vertical cracks: (a) shear wave splitting, (b) V_P anisotropy and (c) V_S anisotropy.

scale of 500-Hz frequency, the layering contributes to shale's VTI anisotropy. This effect is greater for layers having greater contrast in elastic properties. This leads to the fact that the anisotropy found for the 500-Hz frequency scale is of VTI symmetry. The Thomsen parameters found for 500-Hz scale are not too variable in depth compared to those at the scale of sonic measurements. Thus, ε varies from 0.12 to 0.37, γ changes from 0.24 to 0.45 and δ ranges from 0.06 to 0.12. However, the average values of the Thomsen parameters are very close to those found at the scale of sonic frequencies for shale without vertical cracks.

The inversion technique proposed makes it possible to estimate the effect of the bound water on the stiffness tensor of illite, which produces a difference in properties of illite monocrystal compared to '*in situ*' illite. The components found for the stiffness tensor of

'*in situ*' illite are (in GPa): $C_{11} = 127.4$, $C_{33} = 54.7$, $C_{44} = 14.4$, $C_{66} = 39.7$ and $C_{13} = 28.4$.

ACKNOWLEDGMENTS

This work was performed under financial support of Devon Energy, Inc. The authors thank John Queen, Sven Treitel, Roger Slatt, Ray Brown, Charles Mankin, William Menke, Mark Chapman, Siska Valcke and Mike Kendall for their comments and suggestions which definitely improved the paper.

REFERENCES

Backus, G.E., 1962. Long-wave elastic anisotropy produced by horizontal layering. *J. geophys. Res.,* **67,** 4427–4440.

Bayuk, I. & Chesnokov, E., 1998. Correlation between elastic and transport properties of porous cracked anisotropic media, *J. Phys. Chem. Earth,* **23**(3), 361–366.

Bayuk, I., Vikhorev, A., Hooper, J., Tertychnyi, V., Kukharenko, Yu. & Chesnokov, E., 2003a. Frequency Dependent Effects in Porous Rocks, *Int. Geophys. Conf. "Geophysics of 21 Century–The Leap into Future"*, Moscow, 1–4 September, 2003, PS10. Extended Abstracts on CD-ROM.

Bayuk, I., Vikhorev, A., Hooper, J. & Chesnokov, E., 2003b. Correlation Function Behavior in Productive and Nonproductive Layers, *Int. Geophys. Conf. "Geophysics of 21 Century–The Leap into Future"*, Moscow, 1–4 September, 2003, PS1. Extended Abstracts on CD-ROM.

Bayuk, I., Ammerman, M. & Chesnokov, E., 2007. Elastic moduli of anisotropic clay, *Geophysics,* **72,** D107–117.

Brie, A. *et al.*, 1998. New directions in sonic logging, *Oilfield Rev.,* 40–53.

Chapman, M., 2003. Frequency-dependent anisotropy due to meso-scale fractures in the presence of equant porosity, *Geophys. Prospect.,* **51,** 369–379.

Hornby, B.E., Schwartz, L.M. & Hudson, J.A., 1994. Anisotropic effective-medium modeling of the elastic properties of shales, *Geophysics,* **59,** 1570–1583.

Hudson, J.A., 1981. Wave speeds and attenuation of elastic waves in material containing cracks, *Geophys. J. R. Astr. Soc.,* **64,** 133–150.

Johnston, J.E. & Christensen, N.I., 1995. Seismic anisotropy of shales, *J. geophys. Res.,* **B4,** 5991–6003.

Jones, L.E.A. & Wang, H.F., 1981. Ultrasonic velocities in Cretaceous shales from the Williston Basin, *Geophysics,* **46,** 288–297.

Kaarsberg, E.A., 1959. Introductory studies of natural and artificial argillaceous aggregates by sound propagation and x-ray diffraction methods, *J. Geol.,* **67,** 447–472.

Katahara, K.W. 1996. Clay minerals elastic properties, *66th SEG Annual Meeting, Expanded Technical Program Abstracts,* RP 1 **4,** 1691–1694.

Kinoshita, N. & Mura, T., 1971. Elastic fields of inclusion in anisotropic media, *Phys. Stat. Sol.* (a), **5,** 759–768.

Li, Y., 2006. An empirical method for estimation of anisotropic parameters in clastic rocks, *Leading Edge,* **6,** 706–711.

Lonardelli, I., Wenk, H.-R. & Ren, Y., 2007. Preferred orientation and elastic anisotropy in shales, *Geophysics,* **72,** D33–D40.

Mura, T., 1991. *Micromechanics of Defects in Solids,* Kluwer Academic Publisher, Dordrecht.

Ponte Castaneda, P. & Willis, J.R., 1995. The effect of spatial distribution on the effective behavior of composite materials and cracked media, *J. Mech. Phys. Sol.,* **43,** 1919–1951.

Rytov, S.M., 1956. Acoustical properties of a thinly laminated medium, *Soviet Phys.: Acoust.,* **2**(1), 68–80.

Sayers, C.M., 1998. Long-wave seismic anisotropy of heterogeneous reservoirs, *Geophys. J. Int.,* **132,** 667–673.

Sayers, C.M., 2005. Seismic anisotropy of shales, *Geophys. Prospect.,* **53,** 667–676.

Shermergor, T.D., 1977. *Theory of Elasticity of Microinhomogeneous Media,* Nauka, Moscow (in Russian).

Valcke, S.L., Casey, M., Lloyd, G.E., Kendall, J.-M. & Fisher, Q.J., 2006. Lattice preferred orientation and seismic anisotropy in sedimentary rocks, *Geophys. J. Int.,* **166,** 652–666.

Vernik, L., 1993. Microcrack-induced versus intrinsic elastic anisotropy in mature HC-source shales, *Geophysics,* **58,** 1703–1706.

Vernik, L., 1994. Hydrocarbon-generation-induced microcraking of source rocks, *Geophysics,* **59,** 555–563.

Vernik, L. & Liu, X., 1997. Velocity anisotropy in shales: a petrophysical study, *Geophysics,* **62,** 521–532.

Wang, Z., Wang, H. & Cates, M.E., 2001. Effective elastic properties of solid clays, *Geophysics,* **66,** 428–440.

Wenk, H.-R., Lonardelli, I., Franz, H., Nihei, K. & Nakagawa, S., 2007. Preferred orientation and elastic anisotropy of illite-rich shale, *Geophysics,* **72,** E69–E72.

Willis, J. 1977. Bounds and self-consistent estimates for the overall properties of anisotropic composites, *Mech. Phys. Sol.,* **25,** 185–202.

APPENDIX

We consider a layered medium and assume that the horizontal symmetry axis of each layer is directed along the Y-axis of laboratory coordinate system and the Z-axis of each layer is directed upward. In this case the equilibrium equations contain only one term in which differentiation is performed for x_3:

$$\sigma_{i3,3} = 0, \tag{A1}$$

where σ is the stress tensor. Comma means differentiation with respect to the variable following the comma. Thus, in A3 the differentiation is performed with respect to x_3.

This gives

$$\sigma_{i3} = \langle \sigma_{i3} \rangle . \tag{A2}$$

Here averaging is performed over a representative volume large enough compared to layer thickness.

By analogy, the condition of strain compatibility yields

$$e_{pr3} e_{qs3} \varepsilon_{rs,33} = 0, \tag{A3}$$

where **e** is the Levi–Civita tensor, and ε is the strain tensor. This gives

$$\varepsilon_{\alpha\beta} = \left\langle \varepsilon_{\alpha\beta} \right\rangle, \ \alpha, \beta = 1, 2. \tag{A4}$$

With the use of (A2) and (A4), the Hooke's law can be written as follows

$$\begin{aligned} \langle \sigma_{3i} \rangle &= (2C_{i3k} - \delta_{3k} C_{3i33}) \, \varepsilon_{3k} + C_{3i\alpha\beta} \left\langle \varepsilon_{\alpha\beta} \right\rangle , \\ \sigma_{\alpha\beta} &= \left(2C_{\alpha\beta 3k} - \delta_{3k} C_{\alpha\beta 33}\right) \varepsilon_{3k} + C_{\alpha\beta\gamma\delta} \left\langle \varepsilon_{\gamma\delta} \right\rangle . \end{aligned} \tag{A5}$$

Here δ is the Kroneker delta.

The first relation of (A5) gives

$$\begin{aligned} \langle \sigma_{33} \rangle &= C_{3333} \varepsilon_{33} + C_{1133} \langle \varepsilon_{11} \rangle + C_{2233} \langle \varepsilon_{22} \rangle , \\ \langle \sigma_{2323} \rangle &= C_{2323} \varepsilon_{23}, \langle \sigma_{13} \rangle = C_{1313} \varepsilon_{13} \end{aligned} \tag{A6}$$

Averaging these relations and using the definition of effective elasticity tensor

$$\left\langle \sigma_{ij} \right\rangle = C^*_{ijkl} \langle \varepsilon_{kl} \rangle , \tag{A7}$$

we have

$$C_{33}^{*} = \left\langle C_{33}^{-1} \right\rangle^{-1}, C_{13}^{*} = \left\langle \frac{C_{13}}{C_{33}} \right\rangle \left\langle C_{33}^{-1} \right\rangle^{-1},$$
$$C_{23}^{*} = \left\langle \frac{C_{23}}{C_{33}} \right\rangle \left\langle C_{33}^{-1} \right\rangle^{-1}, C_{44}^{*} = \left\langle C_{44}^{-1} \right\rangle^{-1}, C_{55}^{*} = \left\langle C_{55}^{-1} \right\rangle^{-1} \quad \text{(A8)}$$

The other four elasticity coefficients are found from the second relation of (A6) and definition (A7). The formulas for the coefficients are as follows:

$$C_{66}^{*} = \left\langle C_{66} \right\rangle, C_{11}^{*} = \langle C_{11} \rangle + \left\langle \frac{C_{13}}{C_{33}} \right\rangle^{2} \left\langle C_{33}^{-1} \right\rangle^{-1} - \left\langle \frac{C_{13}^{2}}{C_{33}} \right\rangle,$$
$$C_{12}^{*} = \langle C_{12} \rangle + \left\langle \frac{C_{13}}{C_{33}} \right\rangle \left\langle \frac{C_{23}}{C_{33}} \right\rangle \left\langle C_{33}^{-1} \right\rangle^{-1} - \left\langle \frac{C_{13} C_{23}}{C_{33}} \right\rangle,$$
$$C_{22}^{*} = \langle C_{22} \rangle + \left\langle \frac{C_{23}}{C_{33}} \right\rangle^{2} \left\langle C_{33}^{-1} \right\rangle^{-1} - \left\langle \frac{C_{23}^{2}}{C_{33}} \right\rangle. \quad \text{(A9)}$$